Int. J. Electrochem. Sci., 8 **(2013)** 5086 - 5101

International Journal of
ELECTROCHEMICAL
SCIENCE
www.electrochemsci.org

Electrochemical Characterization of Ti_5Si_3/TiC Nanocomposite Coating in HCl Solution

Linlin Liu[1], *Jiang Xu*[1,*], *Zhengyang Li*[2,*]

[1] Department of Material Science and Engineering, Nanjing University of Aeronautics and Astronautics, 29 Yudao Street, Nanjing 210016, P.R. China
[2] Institute of Mechanics, Chinese Academy of Sciences, Beijing, 100190, P. R. China
[*]E-mail: xujiang73@nuaa.edu.cn; zhengyang.li@gmail.com

Received: 22 January 2013 / *Accepted:* 28 February 2013 / *Published:* 1 April 2013

A novel Ti_5Si_3/TiC nanocomposite coating was successfully engineered onto Ti-6Al-4V alloy substrate by double glow discharge plasma technique. The microstructure of the newly developed nanocomposite coating was characterized by X-ray diffraction (XRD), scanning electron microscopy (SEM) and transmission electron microscopy (TEM). The results showed that the nanocomposite coating exhibits cauliflower-like structure composed of Ti_5Si_3 grains with an average grain size of ~15 nm and irregular TiC nanoparticles located at the boundaries of cauliflower-like architecture. The electrochemical behavior of the nanocomposite coating and the reference materials (i.e., monolithic Ti_5Si_3 coating and uncoated Ti-6Al-4V alloy) was evaluated in 5 wt.% HCl solution by a variety of electrochemical techniques, including open circuit potential measurement, potentiodynamic polarization, electrochemical impedance spectroscopy and Mott-Schottky analysis. The results revealed that the corrosion resistance of the Ti_5Si_3/TiC nanocomposite coating is slightly lower than that of the monolithic Ti_5Si_3 nanocrystalline coating, but obviously higher than that of uncoated Ti-6Al-4V in 5 wt.% HCl solution.

Keywords: Nanocomposite coating; Electrochemical impedance spectroscopy (EIS); Mott–Schottky analysis;

1. INTRODUCTION

Titanium alloys have a wide range of application in the chemical, petroleum, aerospace and biomedical fields due to their desirable combination of high strength-to-weight ratio, exceptional corrosion resistance and excellent biocompatibility [1, 2]. Unfortunately, the poor tribological properties of titanium alloys have extensively limited their practical applications in numerous engineering components that are often in tribological contact with different metals under stationary or

dynamic load and in relative motion [3, 4]. Moreover, although titanium alloys possess excellent corrosion resistance in many aggressive media, they show a low corrosion resistance in reducing acid or chloride environments [5, 6]. Since the wear and corrosion damage is essentially surface-dependent degradation, the employment of surface modification offers a flexible approach to modify the microstructure and composition of only the near-surface region, thereby improving the wear and corrosion resistance of titanium alloys and extending their service life in harsh environments. To date, a variety of surface modification techniques, such as Micro-plasma oxidation (MPO) [7], plasma immersion ion implantation (PIII) [8], and chemical and physical vapor deposition [9, 10], have been developed. Those modified surface coatings have achieved remarkable success in the improved wear resistance of titanium alloys, but they usually have an adverse effect on corrosion resistance of titanium alloys [9-11]. For instance, Yao and co-workers [7] evaluated the corrosion resistance of ceramic coatings on Ti-6Al-4V alloy prepared by bi-polar micro-plasma oxidation (MPO) technique in a 3.5% NaCl solution. The results showed that these ceramic coatings noticeably deteriorated the corrosion property of Ti-6Al-4V alloy in 3.5% NaCl solution. Yilbas et al. [10] and Razavi et al. [11] also found that the nitrided Ti–6Al–4V alloy is inferior to the uncoated Ti-6Al-4V in the corrosion resistance. Thus, new surface modification technology and coating material system urgently need to be developed for simultaneously improved corrosion and wear resistance of titanium alloys.

In order to meet the ever-increasing demand for the performance of structural materials, transition metal silicides have been the focus of much research in the last years. Among these silicides, monolithic Ti_5Si_3 has received more and more attention recently, because of its satisfactory oxidation resistance, low density (4.32 g/cm^3), high melting point (2130℃) and good creep resistance [12, 13]. In addition, owing to their unique chemical composition and strong, mostly covalent, bonds in crystal structure, Ti_5Si_3 has been recognized as a promising candidate for corrosion-resistant applications. However, due to its complex hexagonal structure with low symmetry and highly covalent bonding, Ti_5Si_3 has inherently poor ductility and fracture toughness at ambient temperature, which is one of the key handicaps for its application reliability. Two most effective approaches to overcome this problem are to form a Ti_5Si_3 matrix composite and reduce its grain size to nanoscale [14]. TiC is an appropriate strengthening phase for the Ti_5Si_3 matrix due to good match thermal expansion between Ti_5Si_3 and TiC (7.7×10^{-6} ℃$^{-1}$ for TiC and 9.7×10^{-6} ℃$^{-1}$ for Ti_5Si_3) [15]. Wang et al. [16] found that fracture toughness of TiC/Ti_5Si_3 composite fabricated by spark plasma sintering was enhanced by more than 50% as compared to monolithic Ti_5Si_3. However, a great deal of research was mainly concentrated on the mechanical properties of Ti_5Si_3-based composites, their electrochemical behaviors remain poorly understood. Limited studies indicated that there has been debate about the effect of reinforcing phase on the corrosion behavior of intermetallic/ceramics-based composite. For example, Gonzalez-Rodriguez et al. [17] reported that the presence of Mo_5Si_3 in Mo_3Si/Mo_5Si_3 composite films was deleterious to corrosion resistance, due to a selective dissolution of the Mo_5Si_3 phase. In contrast, Park et al. [18] suggested that Ti-Si-N coatings composed of nanocrystallite TiN grains embedded in an amorphous SiN_x matrix possessed better corrosion resistance than TiN coatings.

In the current work, novel Ti_5Si_3/TiC nanocomposite coating was prepared onto Ti-6Al-4V alloy substrate by double glow discharge plasma technique. The composition and microstructure of the nanocomposite coating were characterized by X-ray diffraction (XRD), scanning electron microscopy

(SEM) and transmission electron microscopy (TEM). The electrochemical behaviors of the Ti_5Si_3/TiC nanocomposite coating as well as reference materials (i.e., monolithic Ti_5Si_3 coating and uncoated Ti-6Al-4V alloy) were evaluated in 5 wt.% HCl solution through open-circuit potential (OCP) measurement, potentiodynamic polarization and electrochemical impedance spectroscopy (EIS) techniques, and corresponding underlying mechanisms were discussed in terms of the composition and electronic structure of the passive film formed on investigated materials. The primary aim of this work is to explore the effect of TiC on the corrosion resistance of the Ti_5Si_3/TiC nanocomposite coating.

2. EXPERIMENTAL METHOD

2.1. Specimen preparation

The substrate material used is Ti-6Al-4V alloy in the form of discs with a diameter of 40 mm and a thickness of 3 mm. The chemical composition of the alloy in wt.% was: Al: 5.7, V: 3.85, Fe: 0.18, C: 0.038, O: 0.106, N: 0.035 and the balance: Ti. Before deposition, the Ti-6Al-4V substrates were ground using silicon carbide abrasive papers of 2400 grit and mechanically polished with 1.5 μm diamond paste to obtain a mirror-like appearance. The polished substrates were then ultrasonically cleaned in pure alcohol and dried in cold air. The monolithic Ti_5Si_3 nanocrystalline coating and Ti_5Si_3/TiC nanocomposite coating were deposited on the mirror-polished Ti-6Al-4V substrates by a double cathode glow discharge apparatus using two targets with different stoichiometric ratios (i.e., $Ti_{50}Si_{50}$ and $Ti_{40}Si_{40}C_{20}$), respectively. The sputtering targets were fabricated from ball-milled Ti (-300 mesh, >99.9% purity), Si (-200 mesh, >99.5% purity), and C powders (graphite, -500mesh, >99.9% purity) by employing cold compaction under a pressure of 600 MPa. In the deposition process, one cathode is used as the target composed of the desired sputtering materials, and the other cathode is the substrate material. When two different voltages are applied to the two cathodes, glow discharge occurs, as described elsewhere [19].The glow discharge sputtering conditions are as follows: base pressure, 5×10^{-3} Pa; working pressure, 35 Pa; target electrode bias voltage with direct current, -950 V; substrate bias voltage with impulse current, -350 V; substrate temperature, 950℃; target-substrate distance, 10 mm and treatment time 3 h. The composition of the as-prepared coatings may deviate from the that of targets, due to the fact that the composition of the coatings is related not only to the alloy content of target materials, but also to the relative sputtering yields of the alloying elements in the targets. Furthermore, the diffusion of alloying elements at the interface between the coatings and substrates may also affect the composition of the resultant coatings.

2.2. Microstructure characterization and composition analysis

The phase compositions of the as-deposited coatings were studied by X-ray diffractometry (XRD, D8ADVANCE with Cu K□ radiation) operating at 35kV and 40mA. X-ray spectra were collected in the 2θ range from 20° to 90° with a scan rate of 0.05°/s. Metallographic cross-section of the specimens was prepared and etched with the use of Kroll's reagent (10 ml HNO_3, 4 ml HF and 86 ml

distilled water) for 20-30 s. The cross-sectional morphology and chemical composition of the as-deposited coatings were examined by scanning electron microscopy (SEM, Quanta 200, FEI Company) incorporating an X-ray energy dispersive spectroscopy (EDS, EDAX Inc.) analyzer attachment. Transmission electron microscopy (TEM) images were taken by JEOL JEM-2010 at an accelerating voltage of 200 kV. Plane-view samples for TEM observation were prepared using a single-jet electrochemical polishing technique from the untreated side of the substrate. X-ray photoelectron spectroscopy (XPS) measurements were carried out using a Kratos AXIS Ultra ESCA system using Al K□ (1486.71 eV, pass energy of 20 eV). All the binding energy values were calibrated against the C 1s peak of hydrocarbon contamination fixed at 284.8 eV. Peak identification was performed by reference to an XPS database. Survery spectra were recorded on all specimens, followed by high resolution spectra of the Ti 2p, Si 2p and O1s regions. Quantification of the XPS intensities for Ti and Si was carried out using Scofield cross-sections and corrections for the inelastic mean free path of the Ti 2p and Si 2p photoelectrons were used. All binding energies reported have an error in the range of ±0.1 eV.

2.3. Electrochemical measurements

A standard three-electrode electrochemical cell was used for the electrochemical measurements, consisting of test specimen with 1.0 cm^2 exposed area as the working electrode, a saturated calomel electrode (SCE) immersed in saturated KCl solution as the reference electrode, and a large area platinum sheet as the counter electrode. Throughout this paper, all potentials were referred to SCE. All electrochemical measurements were performed at room temperature using an electrochemical workstation Model CHI660b (Shanghai, China) in naturally aerated 5 wt.% HCl solution prepared with analytical grade reagent and distilled water. Prior to the electrochemical measurement, working electrode was initially reduced potentiostatically at -0.80 V for 10 min to remove any previously formed surface film. Immediately following the cathodic pretreatment, the evolution of the open circuit potential (OCP) of test specimens with immersion time was monitored. The testing duration was 30 min with an interval of 2 s. Afterwards, the electrochemical impedance spectroscopy (EIS) measurement was carried out using an excitation signal of 10 mV peak to peak in a frequency domain from 100 kHz down to 10 mHz at the respective OCPs. The EIS experiment data were evaluated and fit to appropriate equivalent circuit using the ZSimpWin software. The potentiodynamic polarization scan was traced at a scan rate of 20 mV/min, starting at -0.30 V more negative than the OCP and scanning in the positive direction. Capacitance measurements for Mott-Schottky analysis were done after the specimens were polarized potentiostatically at a passive potential of 0.80 V for 1 h to form a steady-state passive film. Subsequently, the capacitance of passive film covered specimen was measured at 1000 Hz by stepping the potential in the negative direction from the film formation potential (0.80 V) to -0.30 V in 25 mV increments.

3. RESULTS AND DISCUSSION

3.1. Microstructures and phase analysis

Fig.1 shows the XRD patterns obtained from the as-deposited Ti_5Si_3 nanocrystalline coating and Ti_5Si_3/TiC nanocomposite coating, together with the powder diffraction file data (No. 29-1362) of Ti_5Si_3 (represented by vertical dotted lines).

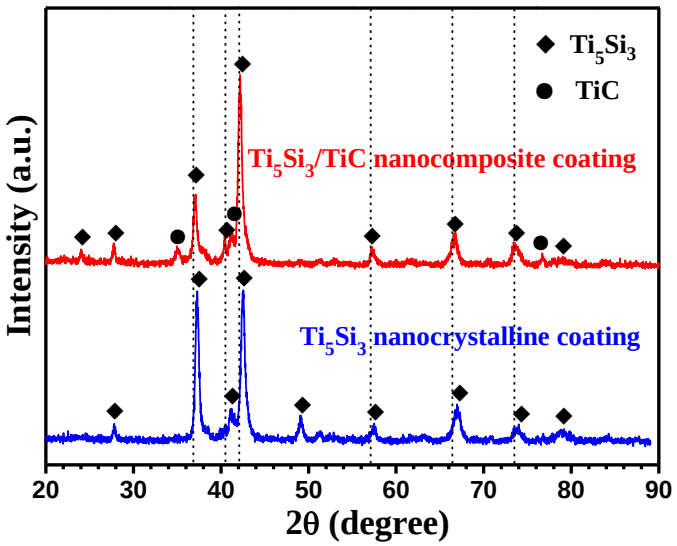

Figure 1. X-ray diffraction patterns obtained from the as-deposited Ti_5Si_3 nanocrystalline coating and Ti_5Si_3/TiC nanocomposite coating.

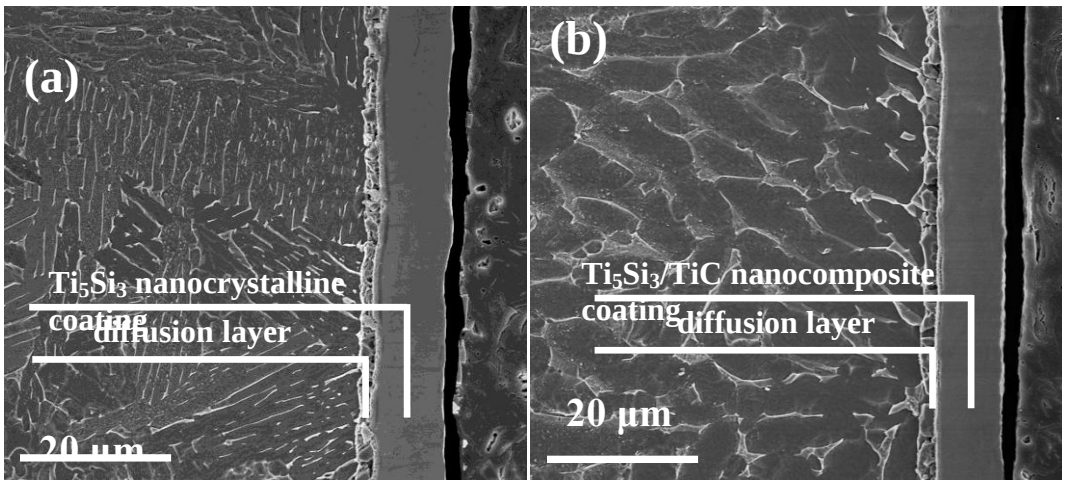

Figure 2. Cross-sectional SEM morphologies of the as-deposited Ti_5Si_3 nanocrystalline coating (a) and Ti_5Si_3/TiC nanocomposite coating (b).

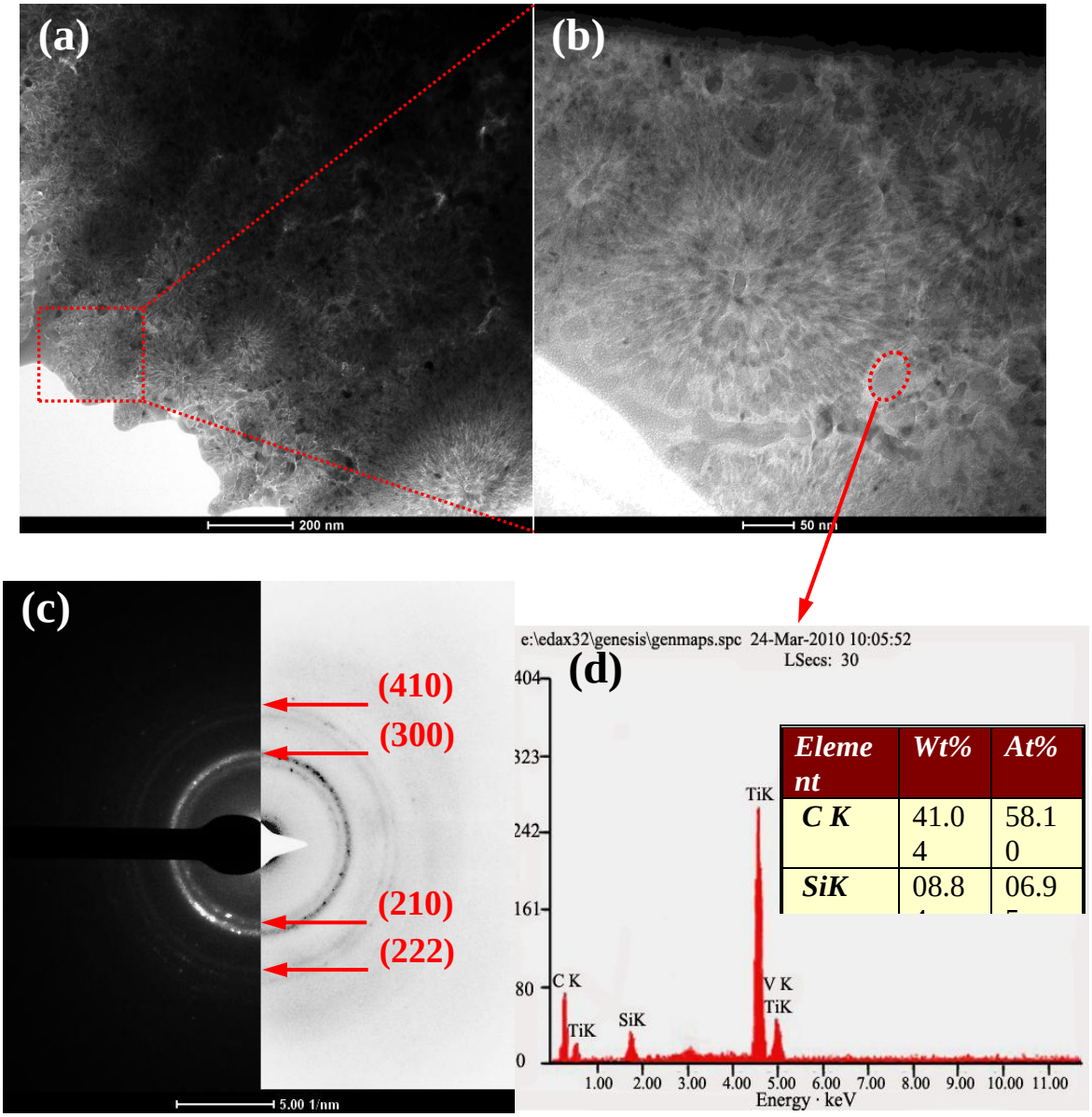

Figure 3. (a) TEM bright-field image of the as-deposited Ti_5Si_3/TiC nanocomposited coating; (b) high magnification image marked in (a); (c) selected area electron diffraction (SAED) pattern of the cauliflower-like structure in (b); (d) energy dispersive X-ray (EDX) spectrum of the particle circled by red dotted lines in (b).

Only one set of broad diffraction peaks corresponding to the hexagonal $D8_8$-structured Ti_5Si_3 has been observed from the XRD pattern taken from the Ti_5Si_3 nanocrystalline coating. For the Ti_5Si_3/TiC nanocomposite coating, additional weak diffraction peaks arising from TiC phase can be detected in addition to the hexagonal $D8_8$-structured Ti_5Si_3 which implies that a small amount of TiC phase exists in the Ti_5Si_3/TiC nanocomposite coating. Moreover, the diffraction peak positions of Ti_5Si_3 in the Ti_5Si_3 nanocrystalline coating shift to the high angle, which indicates the residual tensile stresses being built up in the coating. On the contrary, compared with the powder diffraction file (PDF) data for Ti_5Si_3, the diffraction peak positions of Ti_5Si_3 show little change in the Ti_5Si_3/TiC nanocomposite coating, indicating that carbon can dissolve in Ti_5Si_3 and reduce the residual tensile

stresses in the coating [20].Fig.2 shows the cross-sectional SEM morphologies of the as-deposited Ti_5Si_3 nanocrystalline coating and Ti_5Si_3/TiC nanocomposite coating. Clearly, the two as-deposited coatings are continuous and compact without any visible pores or cavities and combined well with the substrate. Based on a combination of the XRD results and EDS analyses, the two as-deposited coatings can be divided into two different layers: a 10 μm thick outer deposition layer composed of Ti_5Si_3 or Ti_5Si_3/TiC and an inner diffusion layer with a thickness of ~1 μm. Fig.3 shows typical bright-field cross-sectional TEM images obtained from the outer layers of the as-deposited Ti_5Si_3/TiC nanocomposite coating. As shown in Fig.3 (a), the microstructure of this nanocomposite coating is characterized by a cauliflower-like structure with some irregular nanoparticles located at its boundaries. At higher magnification (Fig.3(b)), it is observed that the cauliflower-like structure is in fact composed of many crystallites with an average grain size of ~15 nm, and corresponding selected area electron diffraction (SAED) pattern (Fig. 3(c)) shows diffraction rings matching with those of hexagonal $D8_8$-structured Ti_5Si_3. By combining the XRD and EDS analyses (Fig. 3(c)), these irregular particles with an average grain size of ~15 nm are highly enriched in Ti and C elements and can be resolved as TiC.

3.2. Electrochemical measurements

Fig. 4 presents the evolution of the open circuit potentials of the two coatings and uncoated Ti-6Al-4V alloy immersed in 5 wt.% HCl solution. It is obvious that, for all tested specimens, the overall appearances of the open circuit potential evolution curves are similar in shape, viz, the open circuit potential values quickly increase initially with immersion time towards more anodic values, after which an asymptotical tendency to the approximate steady-state values is distinguished. After 30 min of immersion, the steady-state potentials are 0.135, 0.190 and 0.010 mV for the Ti_5Si_3/TiC nanocomposite coating, Ti_5Si_3 nanocrystalline coating and uncoated Ti-6Al-4V alloy, respectively. The two coatings show higher open circuit potential values, suggesting that they provide an effective corrosion protection to the Ti-6Al-4V substrate. Above open circuit evolutions for all test specimens can be fitted to an exponential decay function with one time constant, and such a time constant can reflect the growth rate of oxide films on the specimens during immersion. Form the fitting results, the time constants of open circuit evolutions for the Ti_5Si_3/TiC nanocomposite coating, Ti_5Si_3 nanocrystalline coating and uncoated Ti-6Al-4V alloy are 2.968, 3.207 and 4.936 min, respectively. Obviously, the two coatings show comparable time constants (≈ 3 min), which are lower than that of uncoated Ti-6Al-4V alloy (≈ 5 min), indicating a higher growth rate of oxide films on the two coatings. Such a phenomenon should be ascribed to the nanocrystalline character of the two as-deposited coatings. Youssef et al. [21] has claimed that the high grain boundary density in nanocrystalline materials facilitated the rapid diffusion of passive elements to the surface and quick formation of a stable passive film.

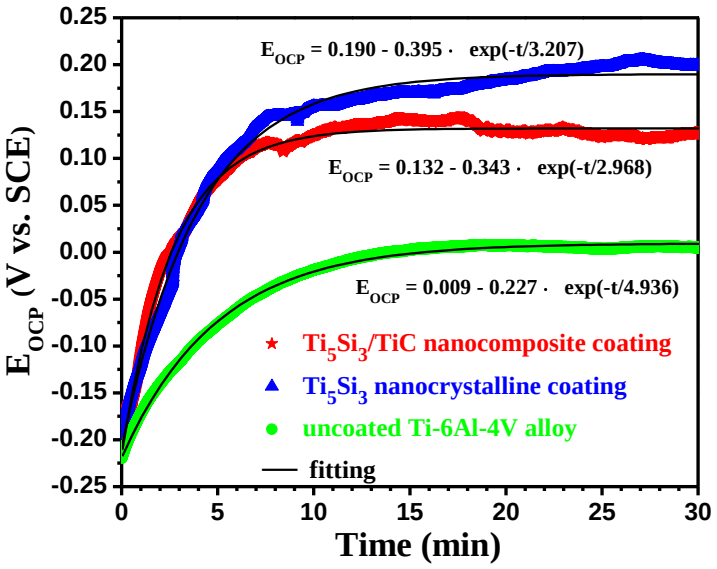

Figure 4. Open circuit potential (OCP) vs. time curves for the Ti_5Si_3 nanocrystalline coating, Ti_5Si_3/TiC nanocomposite coating and uncoated Ti-6Al-4V alloy in 5 wt.% HCl solution.

Fig.5 compares typical potentiodynamic polarization curves of the two coatings and uncoated Ti-6Al-4V alloy in 5 wt.% HCl solution at room temperature, and Table 1 summarizes the corresponding electrochemical parameters derived from the potentiodynamic polarization curves. It is observed that all anodic polarization curves exhibit similar patterns characterized by the regions of active dissolution, passivation and transpassivation, except for different values of their electrochemical parameters (Table 1).

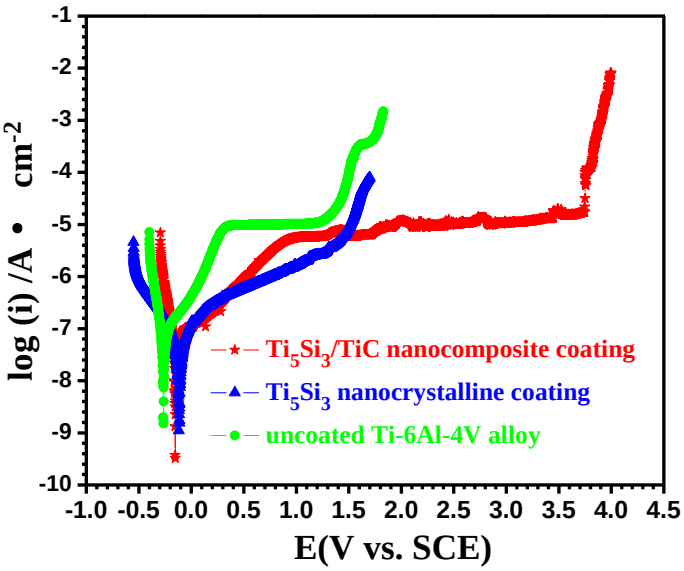

Figure 5. Potentiodynamic polarization curves for the Ti_5Si_3 nanocrystalline coating, Ti_5Si_3/TiC nanocomposite coating and uncoated Ti-6Al-4V alloy in 5 wt. % HCl solution.

Table 1. Electrochemical parameters derived from potentiodynamic polarization curves of investigated specimens in 5 wt.% HCl solution.

Samples	Ti_5Si_3/TiC	Ti_5Si_3	Ti-6Al-4V
E_{corr}(mV)	-153	-117	-264
i_{corr}(μA cm^{-2})	0.054	0.039	0.098
R_p(kΩ cm^2)	621.5	1082.0	386.6
E_{pit}(mV)	～374.8	～160.7	～130.4

This result indicates that the electrochemical processes on the tested specimens are the same. Compared with the uncoated Ti-6Al-4V alloy, the two coatings have a higher corrosion resistance, including lower passive current density (i_{ss}), larger polarization resistance (R_p) and wider passivation potential region. Moreover, more positive corrosion potential (E_{corr}) denotes that the two coatings are more stable in thermodynamic than the uncoated Ti-6Al-4V alloy and can act as an effective protective barrier against corrosion attack. The Ti_5Si_3/TiC nanocomposite coating has slightly negative E_{corr}, lower R_p and larger i_{ss} as compared to the Ti_5Si_3 nanocrystalline coating, reflecting that the presence of TiC phase slightly reduces the corrosion resistance of the Ti_5Si_3/TiC nanocomposite coating. However, the pitting corrosion potential (E_{pit}) of the Ti_5Si_3/TiC nanocomposite coating is significantly higher than that of the Ti_5Si_3 nanocrystalline coating, indicating that the passive film on the Ti_5Si_3/TiC nanocomposite coating exhibits a higher stability.

Fig.6 shows representative impedance spectra of the two coatings and the uncoated Ti-6Al-4V alloy in 5 wt.% HCl solution. The experimental data are presented as symbols, and solid lines correspond to the fitted data using an appropriate equivalent electrical circuit (EEC). Remarkably, in the Nyquist plot (Fig. 6(a)), all tested specimens show similar incomplete capacitive semicircle over the entire frequency range examined except for the difference in the size, reflecting same corrosion mechanism but different rate. Such impedance feature is related to the electrochemical response of an oxide film covered metal electrode. The relatively large capacitive arc for the two coatings reveals that they possess significantly higher electrochemical corrosion resistance than the uncoated Ti-6Al-4V alloy. Bode-magnitude plots (Fig. 6(b)) are also similar in nature for all tested specimens, and they are characterized by two distinct frequency regions. At high frequencies, log|Z| tends to become constant, which is a response typical of the resistive behavior and corresponds to the solution resistance. In the broad middle and low frequency range, the log|Z| vs. log$f$ is a straight line with a slope close to -1, which is characteristic of a predominantly capacitive behavior. Apparently, compared with the uncoated Ti-6Al-4V alloy, the two coatings exhibit wider frequency region related to the capacitive behavior, and higher phase angle maximum, indicative of the formation of the passive films with high insulating properties. Usually, the corrosion rate can be estimated by the value of $|Z|_{f\to 0}$ in the Bode-magnitude plots, and the higher value of $|Z|_{f\to 0}$ signifies a lower corrosion rate of the materials. Hence, the corrosion resistance is the highest for the Ti_5Si_3 nanocrystalline coating, followed by the Ti_5Si_3/TiC nanocomposite coating and uncoated Ti-6Al-4V alloy. An equivalent electrical circuit $R_s(Q_f(R_f(Q_{dl}R_{ct})))$ with two time constants (inset in Fig. 6(a)) was employed to fit the impedance data of Fig. 6, where R_s is the solution resistance between the work electrode and reference electrode, outer subcircuit (R_fQ_f) represents the contribution of the passive film to the impedance in which R_f is the

passive film resistance and Q_f is the constant phase element (CPE) representing the passive film capacitance, while the low frequency parameters R_{ct} and Q_{dl} corresponds to the charge transfer resistance and double layer capacitance, respectively. This model assumes that the passive film is considered as an inhomogeneous and defective layer covering the substrate. In fact, neither real surface of solids in the active range nor passive layers on metallic substrates might be considered as ideally homogeneous [22]. The fitting quality is evaluated by the chi-squared (χ^2) values (shown in Table 2), which is of the order of 10^{-3}, indicating excellent agreement between the measured and the simulated values.

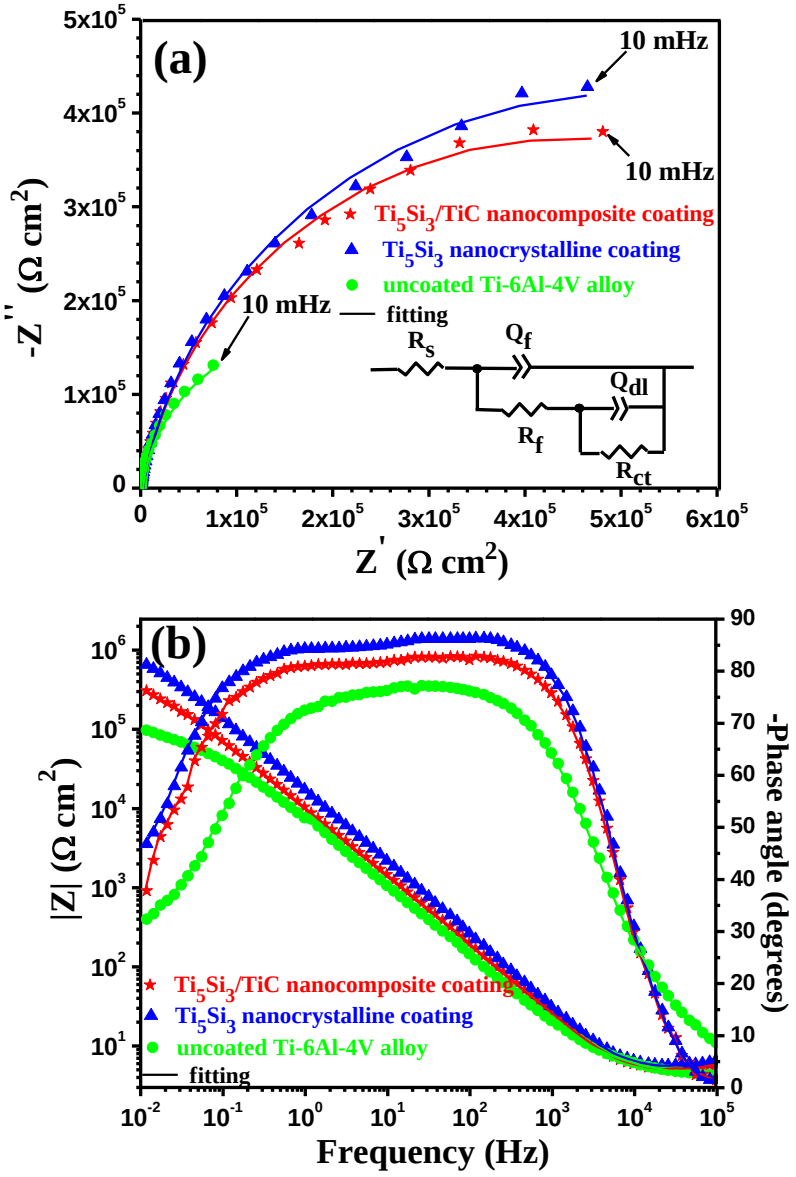

Figure 6. Electrochemical impedance plots for the Ti_5Si_3 nanocrystalline coating, Ti_5Si_3/TiC nanocomposite coating and uncoated Ti-6Al-4V alloy in 5 wt.% HCl solution. (a) Nyquist and (b) Bode plots.

From the fitting circuit parameters (Table 2), it is obvious that, for all tested specimens, the charge transfer resistance (R_{ct}) is more than two order of magnitude larger than the passive film resistance (R_f), implying that the charge transfer process occurring at solution/matrix interface is a rate-determining step of the whole electrochemical process. The charge transfer resistance (R_{ct}) of the Ti_5Si_3/TiC nanocomposite coating is slightly lower than that of the Ti_5Si_3 nanocrystalline coating, but is significantly higher than that of the uncoated Ti-6Al-4V alloy. Since the parameters R and Q are area dependence and cannot be directly used to evaluate corrosion rate, the product R×Q equivalent with the apparent time constant (τ) of relevant electrochemical process was used to eliminate this problem [23, 24]. When one takes a reciprocal of obtained product values, one will receive a rate of relevant electrochemical process. In Table 2, the value of τ_2 caused by the relaxation process of charge transfer reaction is much greater than that of τ_1 related to ionic movement through the passive film, which suggests that the inner subcircuit ($R_{ct}Q_{dl}$) is associated with the slower charge transfer process. The low frequency apparent time constant (τ_2) is the largest for the Ti_5Si_3 nanocrystalline coating (4.205 s^n), followed by the Ti_5Si_3/TiC nanocomposite coating (3.531 s^n) and uncoated Ti-6Al-4V alloy (1.110 s^n). The higher values of τ_2 explain good corrosion protection of the two coatings for the Ti-6Al-4V substrate, which is in a good agreement with the result of potentiodynamic polarization test shown in Fig. 5.

Table 2. Electrochemical parameters fitted from EIS data measured at individual OCP for investigated specimens in 5 wt.% HCl solution.

Samples	Ti_5Si_3/TiC	Ti_5Si_3	Ti-6Al-4V
$R_s(\Omega\ cm^2)$	5.753	6.048	5.527
Q_f-Yo($\Omega^{-1}\ s^n\ cm^{-2}$)	6.983E-6	7.083E-6	6.366E-5
Q_f-n	0.969	0.968	0.950
$R_f(\Omega\ cm^2)$	2475	2821	71.81
$\tau_1(s^n)$	1.728E-2	1.998E-2	4.571E-5
Q_{dl}-Yo($\Omega^{-1}\ s^n\ cm^{-2}$)	3.892E-6	4.083E-6	1.929E-6
Q_{dl}-n	0.776	0.774	0.186
$R_{ct}(\Omega\ cm^2)$	9.073E5	1.030E6	5.752E5
$\tau_2(s^n)$	3.531	4.205	1.110
χ^2	1.09E-3	1.11E-3	3.89E-3

3.3. XPS analysis of passive film composition

XPS analysis was undertaken to provide more information about the component of the passive films. Fig. 7(a) shows XPS survey spectra of the two coatings after potentiostatic polarization at 0.8 V for 1 h in 5 wt.% HCl. As shown in Fig. 7(a), the wide scan spectra exhibit peaks for Ti, Si, O and C peaks. The C 1s peak possibly arises from a contaminant hydrocarbon layer covering the topmost surface of the specimen. The Ti 2p spectrum (Fig. 7(b)) presents one spin orbit doublets Ti $2p_{1/2}$ and Ti $2p_{3/2}$ with the binding energy of 464.3 and 458.5 eV, respectively, which denotes the presence of Ti(IV) [25]. The Si 2p spectrum shown in Fig. 7(c) exhibits a single peak located at a binding energy

of 103.5 eV, corresponding to the Si(IV) oxidation state [26]. In Fig. 7(d), O 1s spectrum can be deconvoluted into two peaks, i.e. at 530.4 and 531.3 eV. According to the literature [27], the peak at 530.4 eV is attributable to the M-O of TiO_2/SiO_2, the other one at 531.3 eV to O-H from the bond water. As a result, the passive films formed on two kinds of as-deposited nanocrystalline coatings consist of TiO_2 and SiO_2, representing a mixed oxide.

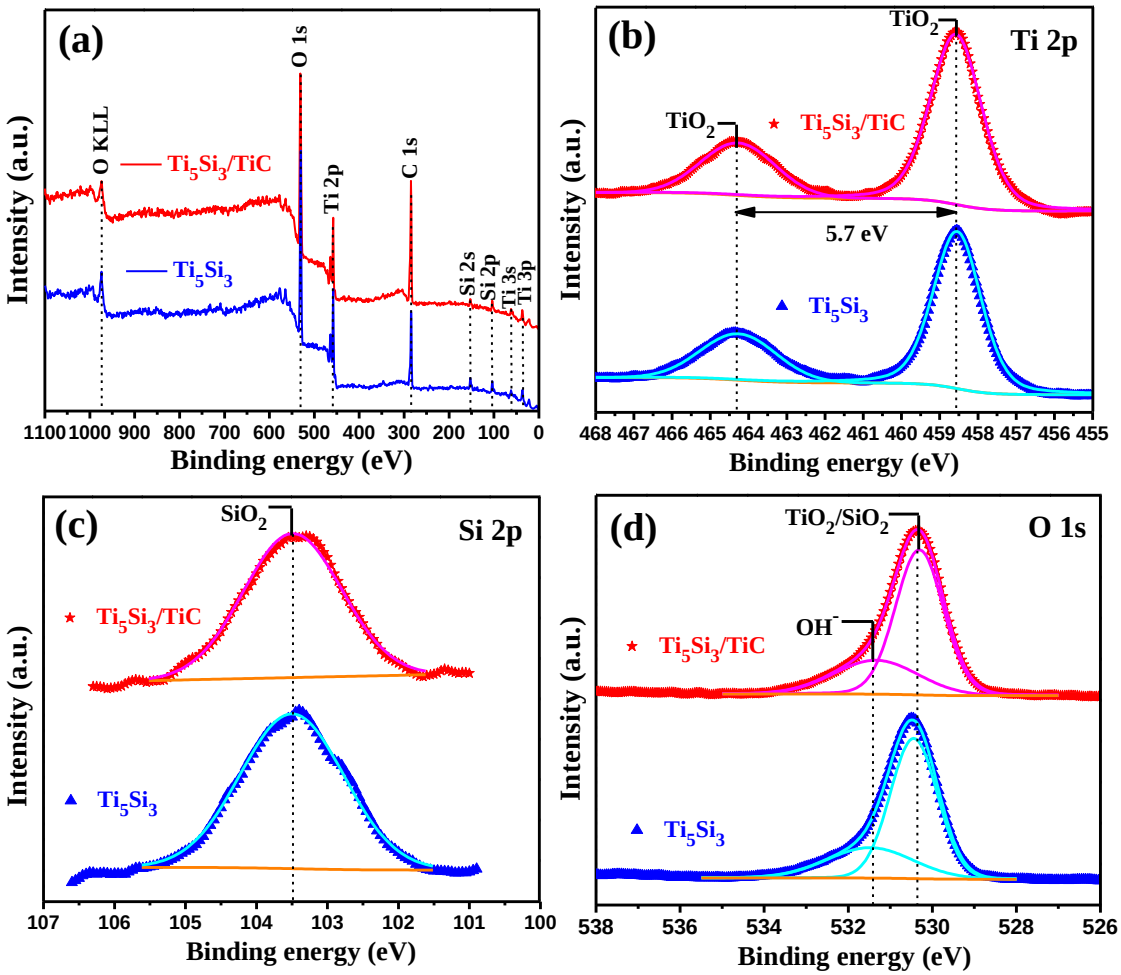

Figure 7. XPS survey spectra and high-resolution XPS spectra of passive films formed on the as-deposited nanocrystalline coatings after potentiostatic polarization at potential of 0.8 V for 1 h in 5 wt.% HCl solution. (a) XPS survey spectra and high-resolution XPS spectra of Ti 2p (b), Si 2p(c) and O 1s.

From quantification of the XPS intensities for Ti 2p and Si 2p, the passive layer formed on the Ti_5Si_3/TiC nanocomposite coating is composed of 64.6 at.% TiO_2 and 35.4 at.% SiO_2, whereas for the Ti_5Si_3 nanocrystalline coating, the passive film composition is 61.8 at.% TiO_2 and 38.2 at.% SiO_2, the later exhibits margially higher SiO_2 content than the former. Since a higher content of SiO_2 in the passive film indicated a higher resistance to corrosion [27], thus, it can be inferred that the Ti_5Si_3 nanocrystalline coating performs the best corrosion resistance, which has been verified by the electrochemical corrosion tests. In fact, two competing and conflicting effects on the passive film

composition are expected. As a second phase existing in the Ti_5Si_3 matrix, the passivity of TiC enables the formation of more TiO_2 in the passive film [28]. On the other hand, preferential bonding of carbon to titanium in the C-doped Ti_5Si_3 matrix ($Ti_5Si_3C_x$), which decreases the activity of Ti while increasing the activity of Si, promotes the formation of SiO_2 in the passive film [29, 30]. As a result, these two opposing effects could cancel each other out, resulting in indistinct difference in the passive film compositions of two as-deposited nanocrystalline coatings.

3.4. Mott-Schottky analysis

The corrosion resistance of passive materials has been found to strongly depend upon the semiconducting electrical properties of the passive film, which can be assessed by measuring the potential dependence of the space charge capacitance, the so-called Mott-Schottky approach [31, 32]. It gives qualitative as to the conductivity type of the semiconductor and quantitative information such as the carrier concentration and flat band potential for the passive film based on the Mott-Schottky equation:

$$\frac{1}{{C_{sc}}^2} = \frac{2}{\varepsilon\varepsilon_0 q N_q A^2}\left(E - E_{fb} - \frac{kT}{q}\right) \qquad (1)$$

where C_{sc} is the space charge capacitance of the passive film, ε the dielectric constant of the passive layer, ε_0 the vacuum permittivity (8.854×10^{-14} F cm^{-1}), q the elementary charge (+e for electrons and –e for holes), N_q the carrier concentration (donor or acceptor), A the electrode surface area (1.0 cm^2 for present study), E the applied potential, E_{fb} the flat band potential, k the Boltzmann constant (1.38×10^{-23} J K^{-1}) and T the absolute temperature (298 K). kT/e may be neglected since it only about 25mV at room temperature. The measured interfacial capacitance, C, is obtained from $C = -1/\omega Z''$, where Z" is the imaginary component of the impedance and $\omega = 2\pi f$ is the angular frequency. Assuming that the capacitance of the Helmholtz double layer (C_{dl}) can be neglected, the measured interfacial capacitance C is equal to the space charge capacitance (C_{sc}) of the passive film.

Fig. 8(a) presents Mott-Schottky plots for the passive films formed on two coatings and uncoated Ti-6Al-4V alloy at 0.8 V for 1 h in 5 wt.% HCl solution. Obviously, linear relations with positive slopes indicate that, for all tested specimens, the passive films behave like n-type semiconductor character. For an n-type semiconductor film, the parameter N_q refers to donor density (N_d) in the space charge region and the donors are usually some positive non-stoichiometric point defects, such as cation interstitials or oxygen vacancies [33, 34]. The values of the dielectric constant (ε), determined based on the mixture rule [35] and the compositions of the passive layer derived from the XPS measurements where a value of 60 [31] and 4.34 [31] were taken for pure TiO_2 and SiO_2 respectively, are 40.3, 38.7 and 60 for the passive films grown on the Ti_5Si_3/TiC nanocomposite coating, the Ti_5Si_3 nanocrystalline coating and uncoated Ti-6Al-4V alloy, respectively. Based on above values, the donor density of the passive film is highest for uncoated Ti-6Al-4V alloy (1.75×10^{20} cm^{-3}), followed by the Ti_5Si_3/TiC nanocomposite coating (8.83×10^{19} cm^{-3}) and the Ti_5Si_3 nanocrystalline coating (6.58×10^{19} cm^{-3}), as shown in Fig. 8(b). Since the donor density measured from the Mott-

Schottky analysis does not correspond to impurity concentration but rather only approximates the stoichiometric point defects (i.e., the oxygen vacancies in the case of n-type semiconducting oxide) in the passive film, the significant difference in N_d observed from Fig. 8(b) reflects obvious change in the amount of oxygen vacancies in the passive film. According to the point defect model (PDM) [33], in a stable passive state, the migration of oxygen vacancies and/or cation vacancies through the passive film governs the whole electrochemical process and hence determines the corrosion resistance of the bare material underneath. In this case, the ion conductivity becomes a main factor to decide the passive current density. It has been found that the higher the carrier density, the greater the passive film conductivity [36, 37]. Moreover, higher N_d would promote, from the viewpoint of energy, the diffusion of aggressive anions such as Cl^- through the passive film to the matrix underneath and the diffusion of metallic cations in the opposite direction [38]. Both processes would accelerate corrosion. Therefore, the significant decrease of donor density for two coatings will be accompanied by an improvement in corrosion resistance, which is in accordance with the results of potentiodynamic polarization and EIS tests.

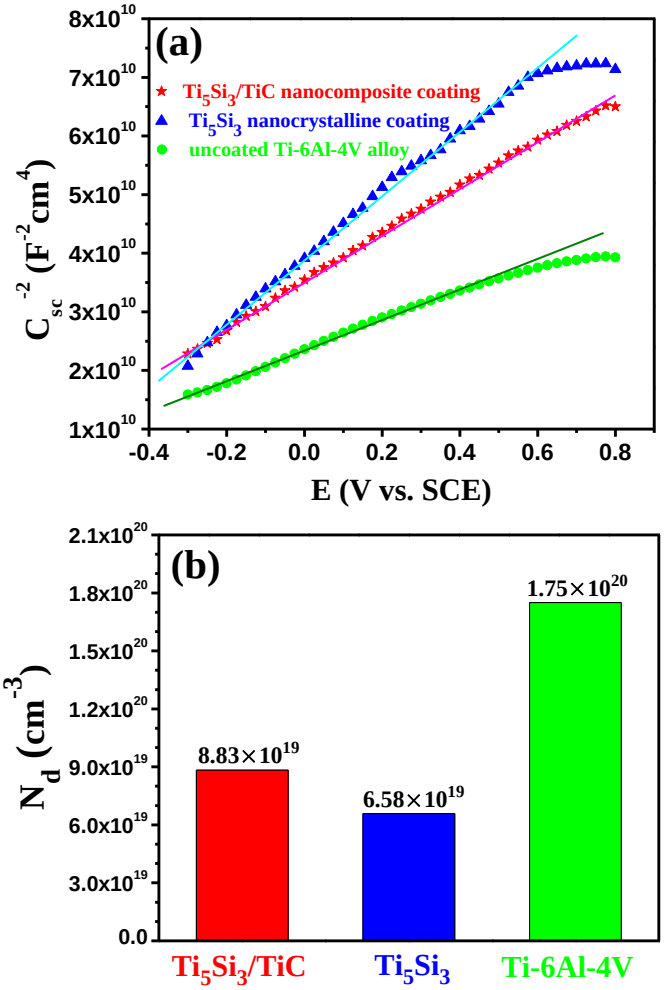

Figure 8. Mott-Schottky plots (a) and donor densities (b) obtained from the passive films formed on two kinds of as-deposited nanocrystalline coatings and uncoated Ti-6Al-4V alloy at 0.8 V for 1 h in 5 wt.% HCl solution.

4. CONCLUSIONS

A novel Ti_5Si_3/TiC nanocomposite coating was successfully engineered onto Ti-6Al-4V alloy substrate by double glow discharge plasma technique. The electrochemical behavior of the newly developed nanocomposite coating and reference materials were comparatively investigated in 5 wt.% HCl solution by various electrochemical techniques. The main conclusions are as follows:

(1) The Ti_5Si_3/TiC nanocomposite coating consists of cauliflower-like Ti_5Si_3 clustered growth domains and irregular TiC nanoparticles distributed at its boundaries. The corrosion resistance of the Ti_5Si_3/TiC nanocomposite coating is slightly lower than that of Ti_5Si_3 nanocrystalline coating, but significantly higher than that of uncoated Ti-6Al-4V alloy.

(2) The passive film formed on the Ti_5Si_3/TiC nanocomposite coating is composed of TiO_2 and SiO_2 phases, and the incorporation of second phase TiC has negligible influence on the composition of the passive film.

(3) Mott-Schottky analysis shows that the passive films formed on all tested specimens exhibit n-type semiconductor behavior, and the donor density of passive film formed on the Ti_5Si_3/TiC nanocomposite coating is comparable to that of the Ti_5Si_3 nanocrystalline coating, and is significantly smaller than that of the uncoated Ti-6Al-4V alloy.

References

1. G.J. Wan, N. Huang, Y.X. Leng, P. Yang, J.Y. Chen, J. Wang and H. Sun, *Surf. Coat. Technol*., 186 (2004) 136.
2. A.P.R. Alves, F.A. Santana, L.A.A. Rosa, S.A. Cursino and E.N. Codaro, *Mater. Sci. Eng*. C, 24 (2004) 693.
3. J.C.H. Hager, J.H. Sandersb and S. Sharma, *Wear*, 265 (2008) 439.
4. D.S. Ming and Y.Z. Wei, *Wear*, 263 (2007) 653.
5. E. Galvanetto, F.P. Galliano, A. Fossati and F. Borgioli, *Corros. Sci*., 44 (2002) 1593.
6. A. Zhecheva, W. Sha, S. Malinov and A. Long, *Surf. Coat. Tech*., 200 (2005) 2192.
7. Z.P. Yao, Z.H. Jiang, S.G. Xin, X.T. Sun and X.H. Wu, *Electrochim. Acta*, 50 (2005) 3273.
8. L.L.G. da Silva, M. Ueda, M.M. Silva and E.N. Codaro, *Surf. Coat. Tech*., 201 (2007) 8136.
9. K.A. Gruss and R.F. Davis, *Surf. Coat. Technol*., 114 (1999) 156.
10. B.S. Yilbas, A.Z. Sahin, Z. Ahmad and B.J. Abdul Aleem, *Corros. Sci*., 37 (1995) 1627.
11. R.S. Razavi, M. Salehi, M. Monirvaghefi and G.R. Gordani, *J. Mater. Process. Tech*., 203 (2008) 315.
12. L. Zhang and J. Wu, *Acta Meter*., 46 (1998) 3535.
13. R. Rosenkranz, G. Frommeyer and W. Smaraly, *Mater. Sci. Eng*. A, 152 (1992) 288.
14. M.H. Enayati, F. Karimzadeh and S.Z. Anvari, *J. Mater. Process.Technol*., 200 (2008) 312.
15. R. Mitra, *Metall. Mater. Transa*. A, 29 (1998) 1629.
16. L.J. Wang, W. Jiang, C. Qin and L.D. Chen, *J. Mater. Sci*., 41 (2006) 3831.
17. J.G. Gonzalez-Rodriguez, I. Rosales, M. Casales, S. Serna and L. Martinez, *Mater. Sci. Eng*., A, 371 (2004) 217.
18. J.H. Park, S.H. Kwon, M.-H. Lee and K.H. Kim, *Electrochem. Solid-State Lett*., 12 (2009) C13.
19. J. Xu, L.L. Liu, X.L. Lu and S.Y. Jiang, *Electrochem. Commun*., 13 (2011) 102.
20. J.J. Williams, M.J. Kramer and M. Akinc, *J. Mater. Res.*, 15 (2000) 1780.
21. Kh.M.S. Youssef, C.C.Koch and P.S.Fedkiw, *Corros. Sci*., 46 (2004) 51.
22. A.I. Muñoz, J.G. Antón, J.L. Guiñón and V.P. Herranz, *Corros. Sci*., 49 (2007) 3200.

23. A. Arutunow and K. Darowicki, *Electrochim. Acta,* 53 (2008) 4387.
24. S. Feliu, J.A. González and J.M. Miranda, V. Feliu, *Corros. Sci*., 47 (2005) 217.
25. Y.J. Zhang, X.F. Li, D. Chen, N.H. Ma, X.S. Hua and H.W. Wang, *Scripta Mater.*, 60 (2009) 543.
26. M.F. López, M.L. Escudero, E. Vida and A.R. Pierna, *Electrochim. Acta*, 42 (1997) 659.
27. Z.L. Jiang, X. Dai and H. Middleton, *Mater. Sci. Eng*. B, 176 (2011) 79.
28. C.M. Alloca, W.S. Williams and A.E. Kaloyeros, *J. Electrochem. Soc*., 134 (1987) 3170.
29. Z.H. Tang, J.J. Williams, A.J. Thom and M. Akinc, *Intermetallics*, 16 (2008) 1118.
30. J.J. Williams, M.J. Kramer, M. Akinc and S.K. Malik, *J. Mater. Res*., 15, (2000), 1773.
31. V.D. Jovic and M.W. Barsoum, *J. Electrochem. Soc.*, 151 (2004) B71.
32. D.G. Li, J.D. Wang and D.R. Chen, *Electrochim. Acta*, 60 (2012) 134.
33. D.D. Macdonald, *J. Electrochem. Soc*., 139 (1992) 3434.
34. J.Q. Kang, Y.F. Yang, X. Jiang and H.X. Shao, *Corros. Sci*., 50 (2008) 3576.
35. P.S. Anjana, M.T. Sebastian, A.-K. Axelsson and N.M. Alford, *J. Eur. Ceram. Soc*., 27 (2007) 3445.
36. E.N. Paleolog, A.Z. Fedotova, O.G. Derjagina and N.D. Tomashov, *J. Electrochem. Soc*., 125 (1978) 1410.
37. D.G. Li, J.D. Wang and D.R. Chen, *J. Power Sources*, 210 (2012) 163.
38. N. Sato, *J. Electrochem. Soc*., 129 (1982) 255.